*Angewandte Chemie International Edition*

Angewandte International Edition Chemie

GDCh German Chemical Society

How to cite: *Angew. Chem. Int. Ed.* **2026**, e4524344
doi.org/10.1002/anie.4524344

RESEARCH ARTICLE OPEN ACCESS

# Harnessing Controlled Dealloying–Support Coupling for Ultrastable PtNi Catalysts in PEMFC Applications

Fei Guo[1] | Manxi Gong[1] | Longxiang Liu[2] | Bochen Li[3] | Ruwei Chen[1] | Mengjun Gong[4] | Wei Zong[1] | Jianuo Chen[3] | Qi Li[5] | Jing Li[5] | Yunpeng Zhong[1] | Zeyi Zhang[6] | Jianrui Feng[1] | Rhodri Jervis[3] | Guanjie He[1]

[1]Department of Chemistry, University College London, London, UK | [2]Department of Materials, University of Oxford, Oxford, UK | [3]Electrochemical Innovation Lab, Department of Chemical Engineering, University College London, London, UK | [4]Department of Chemistry, Imperial College London, White City Campus, London, UK | [5]Department of Chemistry, School of Physical and Chemical Sciences, Queen Mary University of London, London, UK | [6]Department of Chemistry, University of Zurich, Zurich, Switzerland

**Correspondence:** Guanjie He (g.he@ucl.ac.uk)

**Received:** 25 November 2025 | **Revised:** 21 January 2026 | **Accepted:** 28 January 2026

## ABSTRACT

Platinum–transition metal (PtM) alloys are among the most promising oxygen reduction reaction (ORR) catalysts, yet their practical deployment in proton-exchange membrane fuel cells (PEMFCs) is hindered by transition-metal dissolution, particle coarsening, and insufficient durability. Moreover, conventional alloying or intermetallic ordering strategies often aggravate these issues by inducing severe nanoparticle aggregation and instability. Here we report a controllable alloying–dealloying strategy to construct PtNi nanoparticles confined in an N-doped carbon framework ($Pt_1Ni_{1-x}$@$Ni_x$_NC). Ammonia-assisted dealloying produces a Pt-rich shell with an alloyed core, while the N-doped carbon anchors the released Ni atoms form Ni–N/C moieties, thereby suppressing agglomeration and strengthening metal–support interactions. This coordination–support coupling optimizes Pt 5d orbital occupation, weakens oxygen adsorption, and accelerates ORR kinetics. Consequently, $Pt_1Ni_{1-x}$@$Ni_x$_NC exhibits a half-wave potential of 0.932 V and an ultrahigh mass activity of 2.028 A $mgPt^{-1}$, which is 8.75-fold higher than commercial Pt/C and among the best values reported to date for PtNi-based catalysts. Remarkably, it shows only a 6 mV half-wave potential loss after 30,000 cycles, demonstrating exceptional durability. In PEMFCs, the fuel cell delivers 975 mW $cm^{-2}$ peak power density and retains 91.9% of initial performance, underscoring a generalizable approach for designing durable, high-performance low-PGM catalysts for next generation PEMFCs.

## 1 | Introduction

Proton-exchange membrane fuel cells (PEMFCs) have emerged as promising energy-conversion devices owing to their low operating temperature, high efficiency, and environmentally benign operation [1–3]. These advantages position PEMFCs as a critical power source for commercial transportation, offering a sustainable alternative to fossil fuels and accelerating progress toward a carbon-neutral economy [4, 5]. Nevertheless, practical deployment requires electrocatalysts that simultaneously deliver high power density and long-term durability. The performance and lifetime of PEMFCs are largely dictated by the cathode catalyst, where the inherently sluggish oxygen reduction reaction (ORR) remains the principal bottleneck [6–8]. In addition, water generated during the ORR tends to accumulate at the cathode under low-temperature operating conditions, causing electrode flooding if not effectively regulated. Accordingly, the design of cathode electrocatalysts with high intrinsic activity, robust

Fei Guo and Manxi Gong contributed equally to this work.

structural stability, and efficient water management capabilities is essential for enabling the widespread implementation of PEMFCs technologies [9, 10].

To date, most state-of-the-art ORR electrocatalysts are based on platinum (Pt) nanoparticles supported on carbon materials, with commercial Pt/C serving as the benchmark. However, the intrinsic limitations of Pt/C, insufficient catalytic activity, and poor durability continue to hinder large-scale fuel-cell deployment [11]. Alloying Pt with 3d transition metals (M = Co [12, 13], Ni [14, 15], Fe [16, 17]) has emerged as an effective strategy to enhance ORR performance while reducing Pt usage. The incorporation of these transition metals modulates the Pt 5d-band center, optimizes the adsorption energy of oxygenated intermediates, and accelerates ORR kinetics. Yet, under the harsh operating conditions of PEMFCs, these transition metals are prone to dissolution, resulting in progressive degradation of catalytic activity and stability. Moreover, the leached metal ions further impede proton transport within the membrane [18, 19]. To mitigate these drawbacks, ordered PtM intermetallic compounds [20] core-shell Pt@PtM nanostructures [21–24] have been developed, offering improved structural stability and tunable surface electronic properties. Despite their promise, the synthesis of ordered PtM intermetallics remains challenging due to Ostwald ripening during high-temperature annealing, which drives nanoparticle migration and coalescence, ultimately enlarging particle size [25, 26]. Such particle growth drastically reduces the electrochemically active surface area and compromises catalytic performance. Therefore, engineering strong interactions between the nanoparticle catalyst and its support is imperative to suppress over-aggregation during thermal treatment, thereby enabling the formation of highly dispersed, stable, and catalytically active PtM nanostructures [27]. Furthermore, the structural confinement of PtM nanoparticles effectively suppresses nanoparticle migration and agglomeration, ensuring the long-term stability of active sites during prolonged electrochemical cycling in PEMFCs. Recent studies have shown that deliberately constructing interfacial coordination motifs on carbon supports—such as B–N–C moieties in turbostratic carbon or ligand-coordinated metal–carbon interfaces—can effectively immobilize metal species and suppress migration-induced degradation by blocking metal diffusion pathways and stabilizing local coordination environments [28, 29].

Herein, we report a controllable alloying–dealloying strategy to construct PtNi nanoparticles confined within an N-doped carbon matrix (denoted as $Pt_1Ni_{1-x}@Ni_x$_NC). Guided by theoretical predictions, selective ammonia-assisted dealloying transforms disordered PtNi alloys into core–shell nanoparticles featuring a Pt-rich shell and PtNi alloyed core, while simultaneously anchoring dissolved Ni atoms onto the N-doped carbon framework to form Ni_NC moieties. This dual stabilization not only preserves particle dispersion during high-temperature treatment but also optimizes the surface electronic configuration of Pt, thereby accelerating ORR kinetics. Structural and spectroscopic characterizations reveal that this coordinated evolution modulates the Pt 5d orbital occupation, weakens oxygen adsorption, and enhances interfacial water management Benefiting from the synergistic alloy–support coupling, $Pt_1Ni_{1-x}@Ni_x$_NC achieves a half-wave giotential of 0.932 V and a record-high mass activity of 2.028 A $mgPt^{-1}$—8.75 times higher than commercial Pt/C and exceeding most state-of-the-art Pt-based catalysts reported to date. Moreover, in membrane electrode assemblies (MEAs), the catalyst delivers a peak power density of 975 mW $cm^{-2}$ and retains 91.9% of its initial performance after 30,000 cycles, demonstrating exceptional operational robustness under realistic PEMFCs conditions. This work establishes a generalizable pathway that integrates controllable alloying–dealloying chemistry with heteroatom-doped carbon confinement to produce low-PGM catalysts combining unprecedented activity and durability for next-generation fuel-cell technologies.

## 2 | Result and Discussion

To accurately evaluate the catalytic performance of nanoparticles with distinct structural configurations in the four-electron oxygen reduction reaction (ORR), three representative models were constructed: pure Pt, a PtNi intermetallic compound (noted as $Pt_3Ni$), and a PtNi intermetallic core encapsulated by a Pt shell (noted as $Pt@Pt_3Ni$). Density functional theory (DFT) calculations were employed to investigate their electronic structures and to assess the adsorption and desorption characteristics of key ORR intermediates (*OOH, *O, and *OH) along the complete four-electron reaction pathway. This theoretical framework enables a deeper understanding of the structure–property relationships governing the ORR activity and provides guidance for the rational design of high-performance electrocatalysts.

The d-band center serves as a crucial link between the electronic structure of a catalyst and its catalytic performance. To investigate how structural variations in different nanoparticle models influence the d-band characteristics, projected density of states (PDOS) calculations were conducted. These analyses also provide insight into the contributions of individual elements to the total electronic states. As shown in Figure 1a, both $Pt_3Ni$ and $Pt@Pt_3Ni$ exhibit newly formed hybridized electronic states compared to pure Pt. These states likely arise from the interaction between the valence electrons of Pt atoms and the neighboring Ni atoms. Moreover, the overall density of states is noticeably modulated by the nanostructure, with a continuous peak near the Fermi level ($E_F$), suggesting enhanced electrochemical adsorption and desorption capabilities. A notable observation is that in all models, the density of states in the energy region below the $E_F$ (i.e., the occupied states) exhibits higher intensity and greater enrichment compared to the unoccupied states above $E_F$. This indicates that Pt-based nanostructures can supply ample electrons to facilitate the ORR, thus supporting rapid reaction kinetics [30, 31]. In particular, $Pt_3Ni$ and $Pt@Pt_3Ni$ demonstrate significant shifts in their PDOS profiles relative to pure Pt, attributed to strong d-orbital hybridization between Pt and Ni atoms. As illustrated in Figure 1b, this electronic coupling results in a shift of the Pt d-band center ($E_{d\text{-}band}$). For pure Pt, E_d is located at −2.79 eV, while for $Pt_3Ni$, it shifts to −3.36 eV, indicating that more electrons occupy anti-bonding states. Although this enhances the absorption of reaction intermediates, it consequently hinders the desorption. Interestingly, the $E_{d\text{-}band}$ of $Pt@Pt_3Ni$ lies at −3.29 eV, a position that suggests a more balanced electronic environment. This intermediate shift allows for simultaneous optimization of both adsorption and desorption steps in the ORR pathway, thereby promoting favorable reaction kinetics and improved catalytic efficiency. The charge density difference

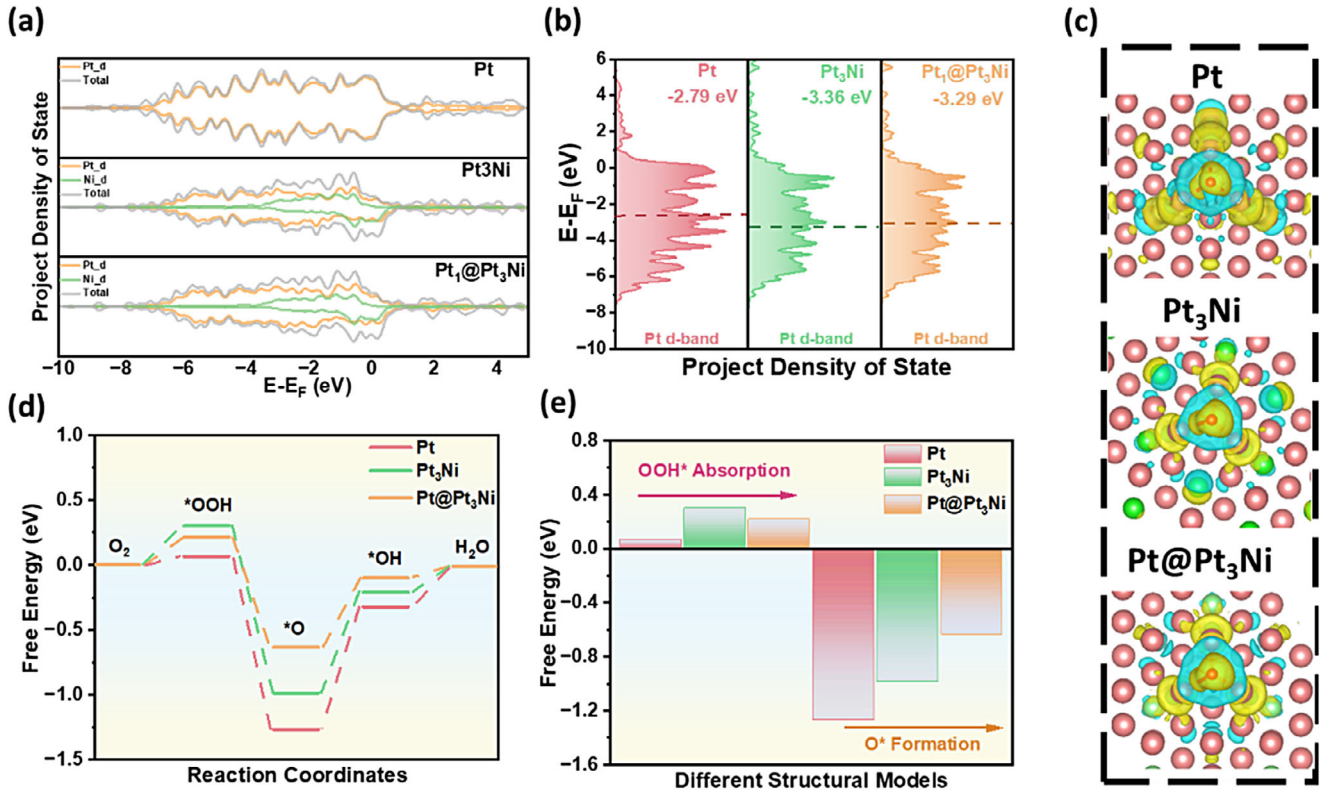


**FIGURE 1** | (a) The total and corresponding d states of Pt, $Pt_3Ni$, and $Pt@Pt_3Ni$. (b) d-Band center of Pt, $Pt_3Ni$, and $Pt@Pt_3Ni$. (c) The electron density difference of Pt, $Pt_3Ni$, and $Pt@Pt_3Ni$, where blue and yellow represent areas of electron diminishing and accumulation; red atoms and green atoms represent platinum and nickel, respectively. (d) Calculated $4e^-$ reaction pathway of ORR on Pt, $Pt_3Ni$, and $Pt@Pt_3Ni$. (e) Corresponding free energy of OOH* absorption and O* formation on different models.

results (Figure 1c) reveal the presence of extensive electron transfer channels between Pt and Ni atoms. Notably, in the $Pt@Pt_3Ni$ structure, a significant accumulation of electrons is observed around the outer-layer Pt atoms. This indicates that structural modulation at the nanoscale enables optimization of the surface electronic configuration of Pt through strong electronic interactions with the underlying Ni, thereby enhancing its catalytic potential.

To evaluate the enhancement in ORR kinetics resulting from structural optimization, free energy diagrams for the four-electron ORR pathway were calculated for Pt, $Pt_3Ni$, and $Pt@Pt_3Ni$ (Figure 1d). For pure Pt, the formation of the *OOH intermediate in the initial step proceeds with relatively low free energy (0.068 eV), indicating a thermodynamically favorable process. However, the subsequent adsorption of *O requires significantly higher energy (−1.268 eV in Figure 1e and Table S1), identifying this step as the rate-determining step (RDS) that limits the overall catalytic efficiency of pure Pt. In contrast, both $Pt_3Ni$ and $Pt@Pt_3Ni$ exhibit stronger *OOH adsorption compared to pure Pt, which suggests more difficult desorption of this intermediate. Nonetheless, they demonstrate substantially lower free energy requirements for the adsorption of *O (−0.986 and −0.634 eV for $Pt_3Ni$ and $Pt@Pt_3Ni$, respectively), indicating a reduced energy barrier for the RDS. Notably, $Pt@Pt_3Ni$ displays the most favorable overall energy profile along the ORR pathway, with the smallest free energy change among the models studied. These results underscore the critical influence of nanostructure engineering on ORR performances. The unique core–shell architecture of $Pt@Pt_3Ni$, comprising a Pt shell and a $Pt_3Ni$ intermetallic core, modulates the Pt d-orbital electronic structure via strong Pt–Ni electronic coupling. This facilitates electron transfer to the surface Pt active sites, enabling a more balanced adsorption and desorption of ORR intermediates and ultimately promoting more efficient reaction kinetics.

To realize the controllable nanoparticle structures (Figure 1) and enhance the overall electrochemical performances of the catalyst, nitrogen-doped carbon (NC) was employed as the support. NC was derived from the pyrolysis of ZIF-8, uniformly distributed nanostructures with an average diameter of approximately 70 nm were obtained (Figure S1a,b). As shown in the x-ray diffraction (XRD) pattern (Figure S1c), no characteristic diffraction peak corresponding to metallic phases is observed, indicating the absence of crystalline metal particles in NC. This observation is further supported by transmission electron microscopy (TEM) analysis (Figure S1d,e), where both bright-field (BF) and high-angle annular dark-field (HAADF) images reveal no discernible metal nanoparticles. The structural model, illustrated in Figure S1f, suggests that the material consists of a nanocarbon cage featuring a highly porous architecture. As illustrated in Figure 2a, $Pt^{4+}$ and $Ni^{2+}$ cations were introduced into the NC support via an impregnation method, followed by thermal treatment under a $H_2$/Ar atmosphere at 750°C to form PtNi alloy nanoparticles, denoted as $Pt_1Ni_1$@NC. Subsequently, the $Pt_1Ni_1$@NC underwent a second heat treatment under flowing $NH_3$ at 100°C to induce

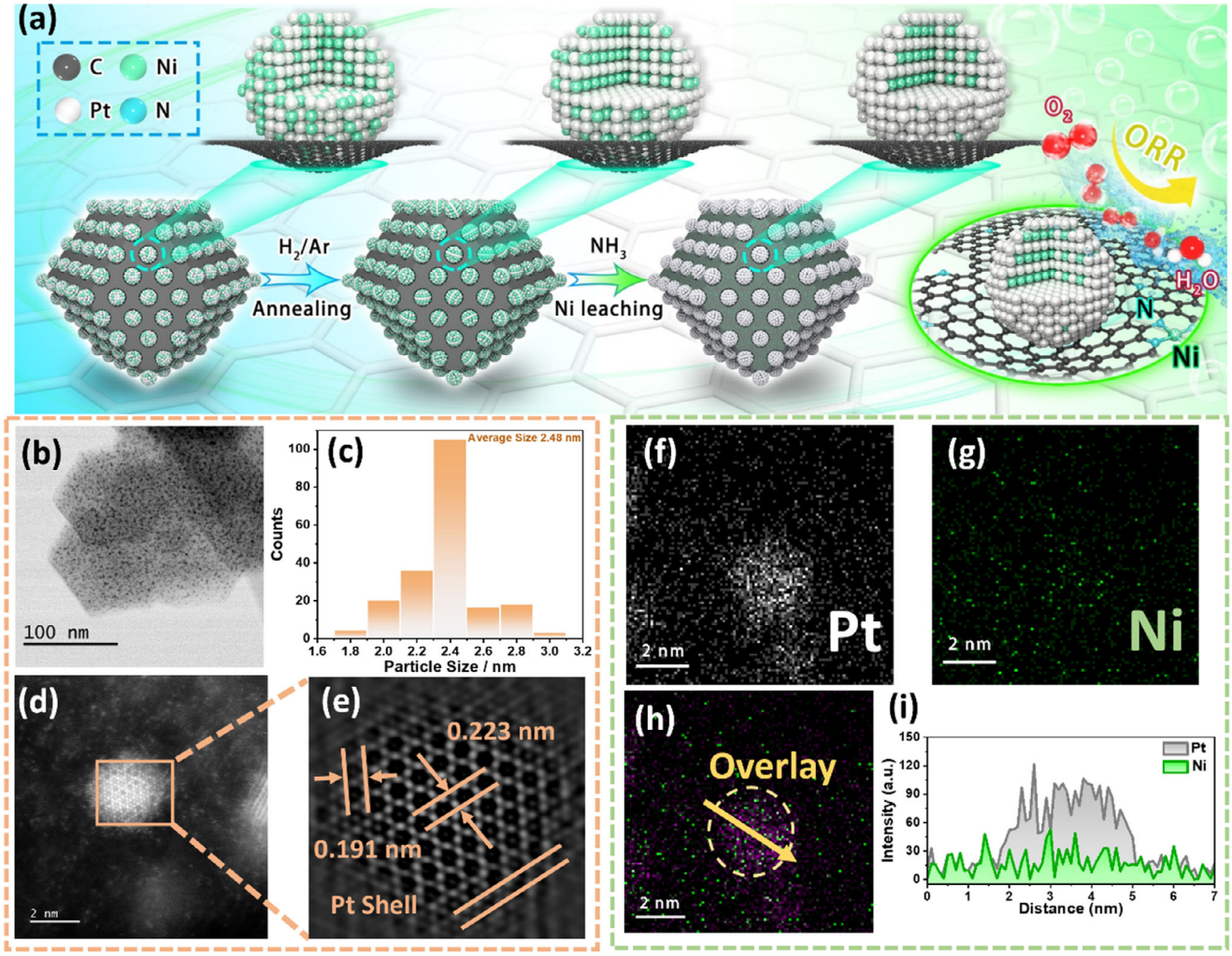


**FIGURE 2** | (a) Schematic illustrations of synthesising $Pt_1Ni_1$@NC and $Pt_1Ni_{1-n}$@$Ni_n$_NC. (b) BF-TEM image of $Pt_1Ni_{1-x}$@$Ni_x$_NC. (c) Size distribution of the nanoparticles from (b). (d) HADDF-STEM image of $Pt_1Ni_{1-x}$@$Ni_x$_NC. (e) Inverse FFT image from (d). (f, g) EDS mapping of Pt and Ni from the nanoparticle of Figure S6b. (h) Overlap mapping of nanoparticles in Figure S6b. (i) Line scan single collected from the yellow arrow of (h).

partial dealloying, designated as $Pt_1Ni_{1-x}$@$Ni_x$_NC. Scanning electron microscopy (SEM) images (Figure S2) reveal that the morphology and particle size of NC support remain largely unchanged after the multi-step thermal treatment, indicating its excellent thermal stability as a support material. Moreover, the absence of discernible nanoparticles on the NC surface suggests that the porous architecture and nitrogen-rich composition of NC effectively suppress the aggregation of PtNi particles during both the alloying and partial dealloying processes. To further investigate the structural evolution, TEM was employed to characterize the $Pt_1Ni_1$ and $Pt_1Ni_{1-x}$ nanoparticles obtained at various synthesis stages. BF-TEM image (Figure S3a) confirms the successful synthesis of uniformly distributed PtNi alloy nanoparticles, with an average diameter of 2.54 nm (Figure S3b), confined within the porous structure of the NC support. High-resolution scanning transmission electron microscopy (HRSTEM) image (Figure S3c), along with the corresponding fast Fourier transform (FFT) patterns (Figure S3d), reveal well-defined atomic arrangements and distinct diffraction spots, indicative of high crystallinity in the PtNi nanoalloys. Further analysis using HAADF imaging (Figure S3e) and inverse FFT (Figure S3f) shows dominant lattice spacings of 0.213 and 0.186 nm, corresponding to the (111) and (200) planes of face-centered cubic (fcc) Pt, respectively. The observed slight lattice contraction is attributed to compressive strain induced by the incorporation of smaller Ni atoms into the Pt lattice during the alloy formation. As shown in the BF-TEM image (Figure 2b), ammonia annealing does not alter the dispersion of the alloy clusters, and the particle size remains uniform, with an average diameter of 2.43 nm (Figure 2c). The HAADF-STEM image (Figure 2d) reveals the presence of surface defects on the nanoparticles, attributed to the selective dissolution and migration of Ni atoms from the PtNi surface under the ammonia atmosphere. Despite this surface restructuring, the inverse FFT image (Figure 2e) indicates that the majority of the nanoparticle lattice remains well ordered, consistent with Figure S4a, while a distinct Pt-rich shell forms at the outer edge. Notably, the measured lattice spacings of $Pt_1Ni_{1-x}$ nanoparticles (0.223 nm and 0.191 nm) are slightly larger than those of $Pt_1Ni$, consistent with the release of compressive lattice strain caused by surface Ni leaching. XRD analysis (Figure S4b) further confirms that the bulk crystal structures of $Pt_1Ni_{1-x}$ and $Pt_1Ni_1$ remain largely unchanged following dealloying, with no significant shift in

peak positions. These results collectively demonstrate that the dealloying process is effectively confined to the nanoparticle surface under the applied synthesis conditions. In addition, it is noteworthy that the Ni atoms dissolved and migrated during ammonia-induced dealloying are not lost from the material but are instead recaptured by the NC support. As highlighted by the red circle in Figure S5a, Ni is uniformly distributed in the vicinity of the $Pt_1Ni_{1-x}$ nanoparticles. The corresponding BF-STEM image (Figure S5b) shows no evidence of aggregated Ni nanoparticles or clusters, indicating that the recaptured Ni is dispersed atomically on the NC surface. This observation is further corroborated by elemental line-scan analysis (Figure S6), which confirms the spatial distribution of Pt and Ni within and around the nanoparticles. As shown in Figure 2f,g, Pt is predominantly enriched at the nanoparticle surface, while Ni exhibits a more diffuse distribution. The overlapped EDS mapping in Figure 2h reveals that the purple regions (overlapping Pt and Ni signals) correspond to the PtNi alloy core, while the green spots surrounding the particles represent Ni atoms redistributed onto the NC support during dealloying. As illustrated in Figure 2i, the linear EDS profile along the yellow arrow (Figure 2h) further confirms a core–shell architecture, with a PtNi alloy core, a Pt-enriched shell, and Ni species dispersed uniformly around the nanoparticles on the carbon matrix.

X-ray photoelectron spectroscopy (XPS) was employed to investigate the surface electronic structure evolution associated with structural changes in the PtNi alloy catalyst. The high-resolution Pt 4f spectrum (Figure 3a) reveals that $Pt_1Ni_{1-x}@Ni_x$_NC exhibits the highest binding energies among the three samples—Pt@NC, $Pt_1Ni_1$@NC, and $Pt_1Ni_{1-x}@Ni_x$_NC. Two distinct Pt 4f doublets are observed at 72.10/75.42 eV and 73.26/76.58 eV (Table S2), corresponding to the $Pt^0$ and $Pt^{2+}$ oxidation states, respectively. In comparison, Pt@NC and $Pt_1Ni_1$@NC show Pt 4f peaks shifted toward lower binding energies. This positive shift in $Pt_1Ni_{1-x}@Ni_x$_NC is attributed to electronic interactions with Ni and structural changes associated with the formation of a core–shell configuration, which leads to an increased Pt 4f binding energy. Moreover, the proportion of metallic $Pt^0$ is significantly enhanced in $Pt_1Ni_{1-x}@Ni_x$_NC, with a $Pt^0/Pt^{2+}$ ratio of 2.63, considerably higher than those of Pt@NC (0.71) and $Pt_1Ni_1$@NC (1.26) (Figure S7), indicating a more electron-rich Pt surface environment. This modulation of the surface electronic structure is further supported by the Ni 2p XPS spectra (Figure 3b, Table S3). In $Pt_1Ni_{1-x}@Ni_x$_NC, the Ni 2p peaks exhibit a negative shift compared to Ni@NC, consistent with the trend observed in the Pt 4f spectra. This shift confirms strong electronic interactions between Pt and Ni, which are further enhanced after dealloying and core–shell structure formation. Notably, three characteristic Ni 2p features are observed in Figure 3b, corresponding to $Ni^0$, $Ni^{2+}$ (from partially oxidized Ni species), and another $Ni^{2+}$ species likely associated with nitrogen coordination in the NC support, indicating the coexistence of multiple chemical states of Ni in the system.

X-ray absorption near-edge spectroscopy (XANES) and extended x-ray absorption fine structure (EXAFS) measurements were carried out to probe the electronic structure and local coordination environment of PtNi nanoparticles before and after dealloying (Figure S8). The Pt $L_3$-edge XANES of $Pt_1Ni_{1-x}@Ni_x$_NC exhibits the most intense white line among all samples, surpassing that of $Pt_1Ni_1$@NC and Pt foil, indicative of a substantially modified Pt surface electronic configuration (Figure 3c), in agreement with the XPS analysis (Figure 3a). A positive shift in the second-derivative spectrum (Figure S9) further points to a higher density of unoccupied Pt 5d states, arising from selective dealloying and enhanced metal–support interactions. This electronic redistribution modulates the surface Pt coordination environment and optimizes the adsorption behavior of oxygenated intermediates toward the Sabatier optimum, thereby promoting ORR kinetics [32]. At the Ni K-edge (Figure 3d), the absorption energies of $Pt_1Ni_{1-x}@Ni_x$_NC and $Pt_1Ni_1$@NC lie between those of Ni foil and NiO, accompanied by a slight negative shift, suggesting an increase in the Ni oxidation state and strong Pt–Ni electronic coupling following dealloying. EXAFS analysis of the Pt $L_3$-edge (Figure 3e) reveals a contraction of the Pt–metal bond length (around 2.64 Å) relative to Pt foil (2.72 Å), arising from lattice compression upon Ni incorporation and additional surface stress induced by Ni segregation after dealloying.

Changes in the Ni K-edge EXAFS are even more pronounced (Figure 3f). Both $Pt_1Ni_{1-x}@Ni_x$_NC and $Pt_1Ni_1$@NC display markedly diminished Ni–Ni and Ni–O features compared to standards, alongside the emergence of a broad feature at 1.6 Å, attributable to Ni–N/C coordination formed post-dealloying. The formation of Ni–N/C moieties is governed by a combination of thermodynamic preference and kinetic confinement. Thermodynamically, nitrogen functionalities exhibit strong coordination affinity toward Ni species, whereas kinetically, the released Ni is rapidly immobilized by abundant N sites [33], effectively suppressing long-range diffusion and re-alloying with Pt. This interpretation is corroborated by the atomically dispersed Ni distribution observed in aberration-corrected electron microscopy. EXAFS fitting of the Pt $L_3$-edge (Figures S10, S11; Table S4) shows a reduced Pt–Pt coordination number, clear evidence of Pt–Ni bonding, and additional Pt–C/N/O contributions arising from interaction with the NC support. Transmission-mode XAS further reveals decreased Pt–Pt and Pt–Ni coordination numbers and increased Pt–C/N/O coordination, mirroring the intensified Pt white-line feature. Notably, Ni K-edge fitting (Figures S12, S13; Table S5) confirms highly dispersed Ni atoms with negligible Ni–Ni coordination and enhanced Ni–C/N/O bonding, the latter shorter than typical Ni–O distances, reflecting strong metal–support interactions and Ni release during dealloying. Wavelet-transform k-space maps (Figures 3g–i and S14) vividly capture the coordination evolution of Pt and Ni through alloying and dealloying. The coordination evolution revealed by EXAFS provides direct insight into the enhanced durability of $Pt_1Ni_{1-x}@Ni_x$_NC.

ORR measurements were performed to evaluate how coordination structure evolution and electronic optimization induced by alloying–dealloying influence catalytic performance. Cyclic voltammetry (CV) in $N_2$-saturated 0.1 M $HClO_4$ (Figure 4a) shows that the MOF-derived NC possesses a larger electrochemically active surface area and double-layer capacitance than commercial Vulcan carbon. Among all catalysts, $Pt_1Ni_{1-x}@Ni_x$_NC exhibits the most pronounced double-layer feature, reflecting enhanced interfacial electron exchange. Correspondingly, ORR polarization curves (Figures 4b, S15) reveal that $Pt_1Ni_{1-x}@Ni_x$_NC achieves the highest half-wave potential ($E_{1/2}$ at 0.932 V), outperforming $Pt_1Ni_1$@NC (0.910 V), Pt@NC (0.887 V), and commercial Sigma 20wt% Pt/C (0.875 V). The Tafel slope (Figure 4c) further

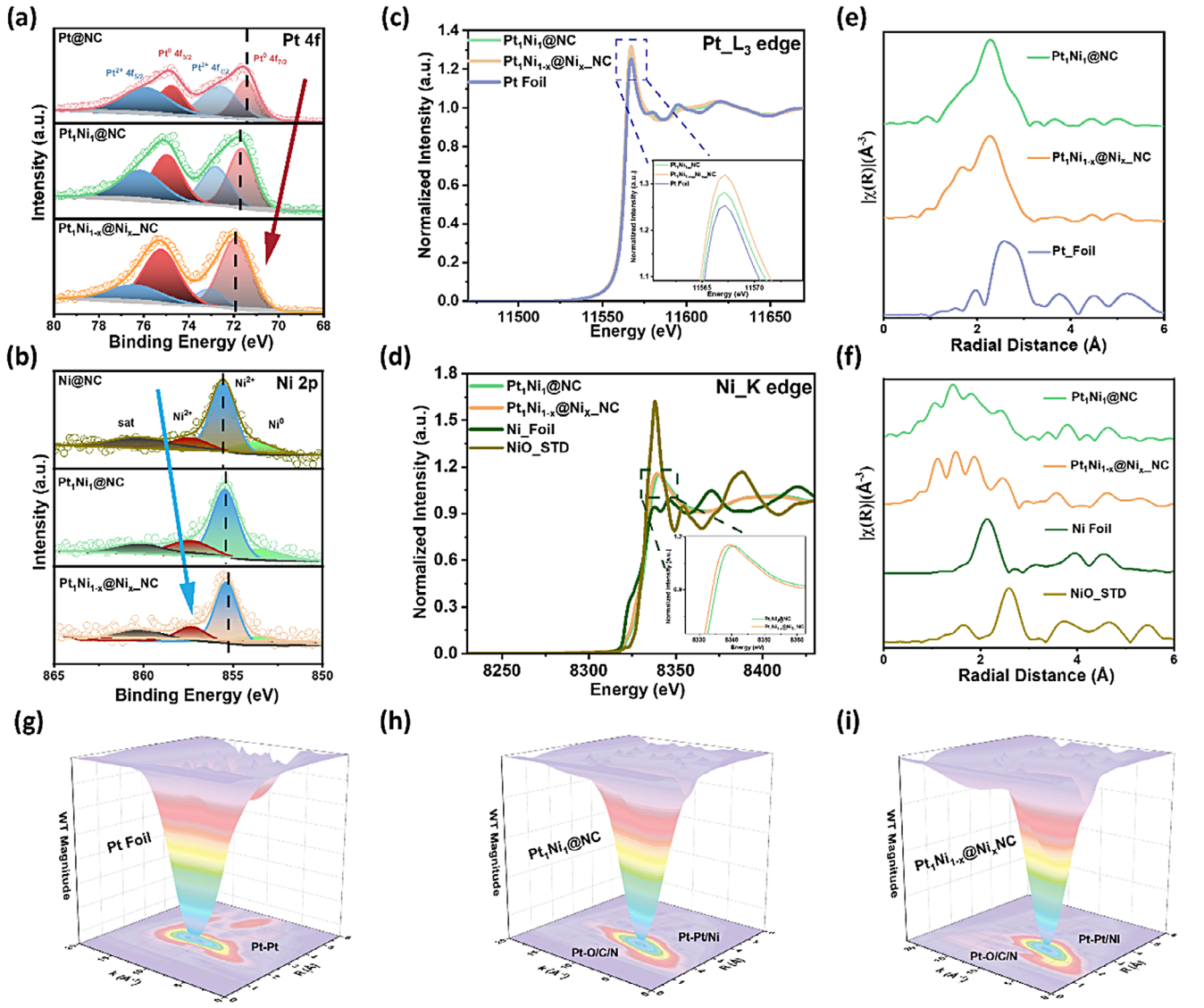


**FIGURE 3** | XPS spectra of (a) Pt 4f of Pt@NC, $Pt_1Ni_1$@NC and $Pt_1Ni_{1-x}$@$Ni_x$_NC. (b) Ni 2p of Ni@NC, $Pt_1Ni_1$@NC and $Pt_1Ni_{1-x}$@$Ni_x$_NC. XANES spectra of (c) Pt_$L_3$ edge XANES of Pt Foil, $Pt_1Ni_1$@NC and $Pt_1Ni_{1-x}$@$Ni_x$_NC (inset: enlarged absorption near edge peak of Pt_$L_3$). (d) Ni_K edge XANES of Ni foil, NiO, $Pt_1Ni_1$@NC, and $Pt_1Ni_{1-x}$@$Ni_x$_NC (inset: enlarged absorption near edge peak of Ni_K edge for $Pt_1Ni_1$@NC and $Pt_1Ni_{1-x}$@$Ni_x$_NC). (e) the $k^2$-weighted $X(k)$-function of the Pt $L_3$-edge EXAFS spectra from (c). (f) The $k^2$-weighted $X(k)$-function of the Ni K edge EXAFS spectra from (d). (g–i) WT-EXAFS contour maps of the Pt $L_3$-edge for Pt foil, $Pt_1Ni_1$@NC, and $Pt_1Ni_{1-x}$@$Ni_x$_NC.

confirms the accelerated kinetics, with $Pt_1Ni_{1-x}$@$Ni_x$_NC exhibiting the lowest value (58.6 mV $dec^{-1}$), consistent with its superior turnover frequency (Figure S16). These results demonstrate that structural evolution during dealloying optimizes ORR kinetics and enhances catalytic activity. To further probe the structure–activity relationship, $Pt_1Ni_{1-2x}$@$Ni_{2x}$_NC and $Pt_1Ni_{1-3x}$@$Ni_{3x}$_NC were synthesized for comparison. As shown in Figures 4d and S17–S19, their $E_{1/2}$ values (0.912 and 0.902 V, respectively) and Tafel slopes (58.9 and 59.6 mV $dec^{-1}$, respectively) are inferior to $Pt_1Ni_{1-x}$@$Ni_x$_NC, underscoring the unique advantage of its optimized coordination environment in boosting ORR activity. Consistently, $Pt_1Ni_{1-x}$@$Ni_x$_NC also exhibits a higher turnover frequency, indicating intrinsically enhanced reaction kinetics at the active Pt sites. Further XPS analysis (Figure S20 and Tables S6, S7) reveals that with increasing dealloying temperature, the binding energies of $Pt^0$ and $Pt^{2+}$ in $Pt_1Ni_{1-2x}$@$Ni_{2x}$_NC (71.98/75.30 eV and 73.14/76.46 eV) and $Pt_1Ni_{1-3x}$@$Ni_{3x}$_NC (71.71/75.03 eV and 72.87/76.19 eV) shift to lower values compared to those in $Pt_1Ni_{1-x}$@$Ni_x$_NC (72.10/75.42 eV and 73.26/76.58 eV), while the corresponding Ni 2p binding energies increase. This trend indicates that elevated dealloying temperatures alter the surface chemical states of Pt and Ni and weaken their intermetallic electronic interactions. To further probe these effects, XAS was employed to analyze the structural and coordination evolution. As shown in Figure 4e,f, the Pt $L_3$-edge white-line intensity gradually decreases with increasing dealloying temperature, whereas the Ni K-edge intensity first increases and then decreases. Such behavior likely arises from further dissolution of Ni atoms followed by their partial reaggregation on the support. This interpretation is supported by EXAFS analysis (Figures S21–S23; Tables S8, S9), which shows that the Pt–Pt coordination number increases in $Pt_1Ni_{1-2x}$@$Ni_{2x}$_NC (5.4) and $Pt_1Ni_{1-3x}$@$Ni_{3x}$_NC (5.6) compared with $Pt_1Ni_{1-x}$@$Ni_x$_NC (5.3), while the Pt–Ni coordination number decreases, confirming the progressive release of

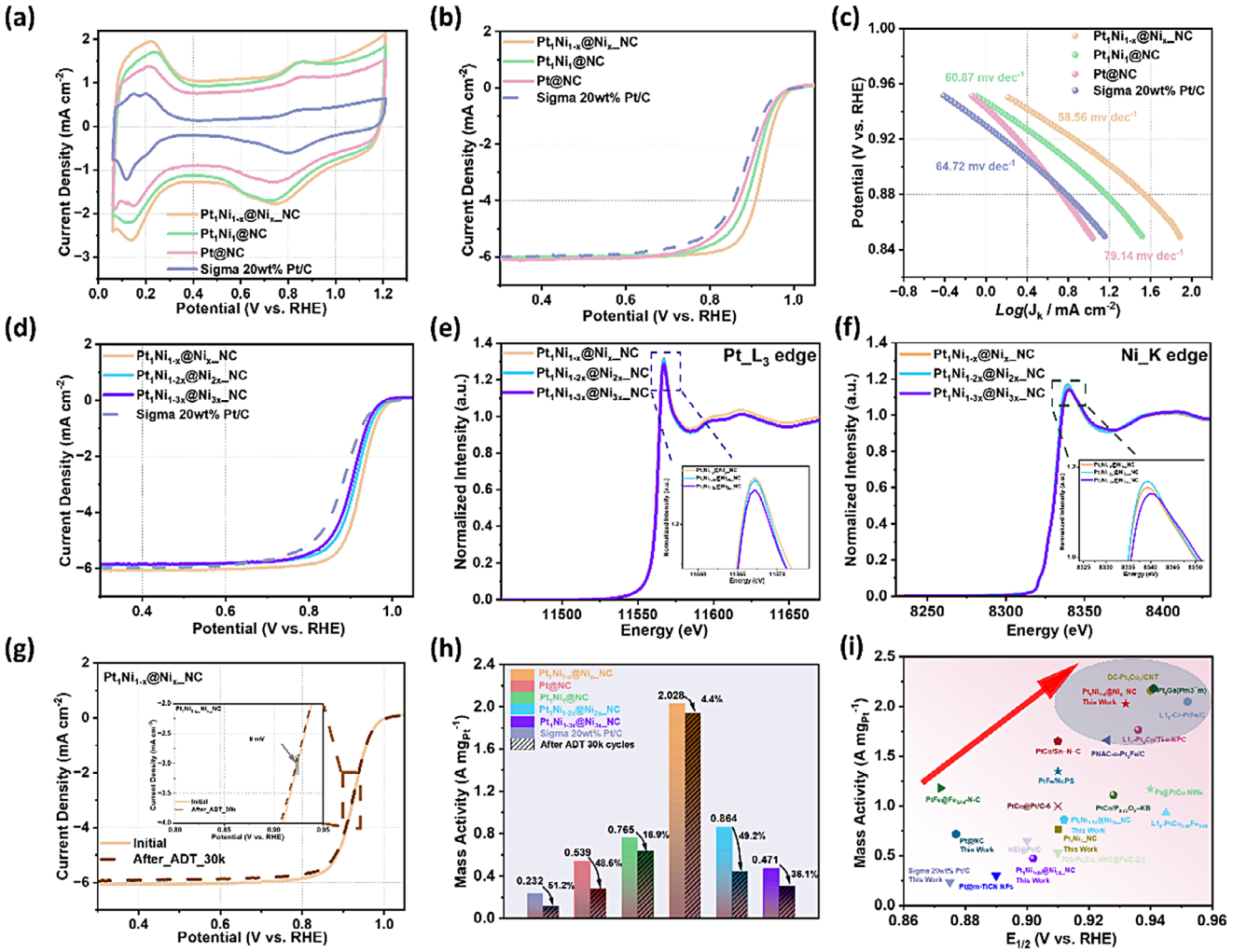


**FIGURE 4** | (a) $N_2$-saturated CV curves, (b) $O_2$-saturated ORR polarization curves, (c) Tafel slope of Pt@NC, $Pt_1Ni_1$@NC, $Pt_1Ni_{1-x}$@$Ni_x$_NC, and Sigma 20wt% Pt/C. (d) $O_2$-saturated ORR polarization curves of $Pt_1Ni_{1-x}$@$Ni_x$_NC, $Pt_1Ni_{2-x}$@$Ni_{2x}$_NC, $Pt_1Ni_{1-3x}$@$Ni_{3x}$_NC, and Sigma 20wt% Pt/C. (e) Pt_$L_3$ edge XANES (inset: enlarged absorption near edge peak of Pt_$L_3$), (f) Ni_K edge XANES (inset: enlarged absorption near edge peak of Ni_K) of $Pt_1Ni_{1-x}$@$Ni_x$_NC, $Pt_1Ni_{2-x}$@$Ni_{2x}$_NC, and $Pt_1Ni_{1-3x}$@$Ni_{3x}$_NC. (g) ORR polarization curves before and after 30k ADT cycles of $Pt_1Ni_{1-x}$@$Ni_x$_NC (inset: enlarged half-wave overpotential position). (h) mass activity at 0.9 V versus RHE of all samples. (i) Mass activity and half-wave overpotential comparison among electrocatalysts in this work and other recently reported Pt-based electrocatalysts. All electrochemical tests were carried out in 0.1 M $HClO_4$.

Ni atoms from the PtNi alloy at higher dealloying temperatures. Meanwhile, the Ni–Ni coordination number first decreases and then increases, whereas the Ni–C/N/O coordination number exhibits the opposite trend, consistent with the reaggregation of Ni atoms onto the support, as also reflected in the Ni K-edge features (Figure 4f).

Accelerated durability testing (ADT, Figure S24) demonstrated that $Pt_1Ni_{1-x}$@$Ni_x$_NC exhibits superior catalytic stability. Its ORR polarization curve remained essentially unchanged after 30,000 cycles, with a half-wave potential loss of only 6 mV (Figure 4g). Normalized ORR activities further highlight its outstanding performance, $Pt_1Ni_{1-x}$@$Ni_x$_NC achieves a mass activity of 2.028 A $mg_{Pt}^{-1}$, surpassing $Pt_1Ni_1$@NC, Pt@NC, $Pt_1Ni_{1-2x}$@$Ni_{2x}$_NC, $Pt_1Ni_{1-3x}$@$Ni_{3x}$_NC, and Sigma 20wt% Pt/C by factors of 2.65, 2.82, 2.35, 4.31, and 8.75, respectively (Tables S10–S11, Figure 4h). Importantly, the mass activity decays by only 4.4% after ADT, underscoring its remarkable durability (Figure S25). The enhanced activity and stability of $Pt_1Ni_{1-x}$@$Ni_x$_NC can be attributed to strengthened Pt–Ni intermetallic interactions arising from coordination restructuring under optimized dealloying conditions, while stabilized Pt coordination suppresses atomic rearrangement and particle coarsening. In parallel, immobilization of released Ni as Ni–N/C moieties block dissolution–migration pathways, collectively accounting for the excellent long-term stability (Tables S4, S5, S8, and S9). Compared with state-of-the-art catalysts, $Pt_1Ni_{1-x}$@$Ni_x$_NC occupies a leading position in ORR performance (Figure 4i).

While RDE measurements reflect intrinsic ORR kinetics under idealized mass-transport conditions, MEA performance is additionally governed by catalyst–ionomer interactions, gas diffusion, and water management within the electrode architecture. Further, the catalysts' membrane electrode assembly (MEA) performance was assessed under practical fuel cell operating conditions (cathode catalyst loading: 0.1 $mg_{Pt}$ $cm^{-2}$, 80°C, 150 $kPa_{abs}$ backpressure; Figures 5a and S26). Humidity-dependent MEA tests revealed excellent tolerance: the peak power density

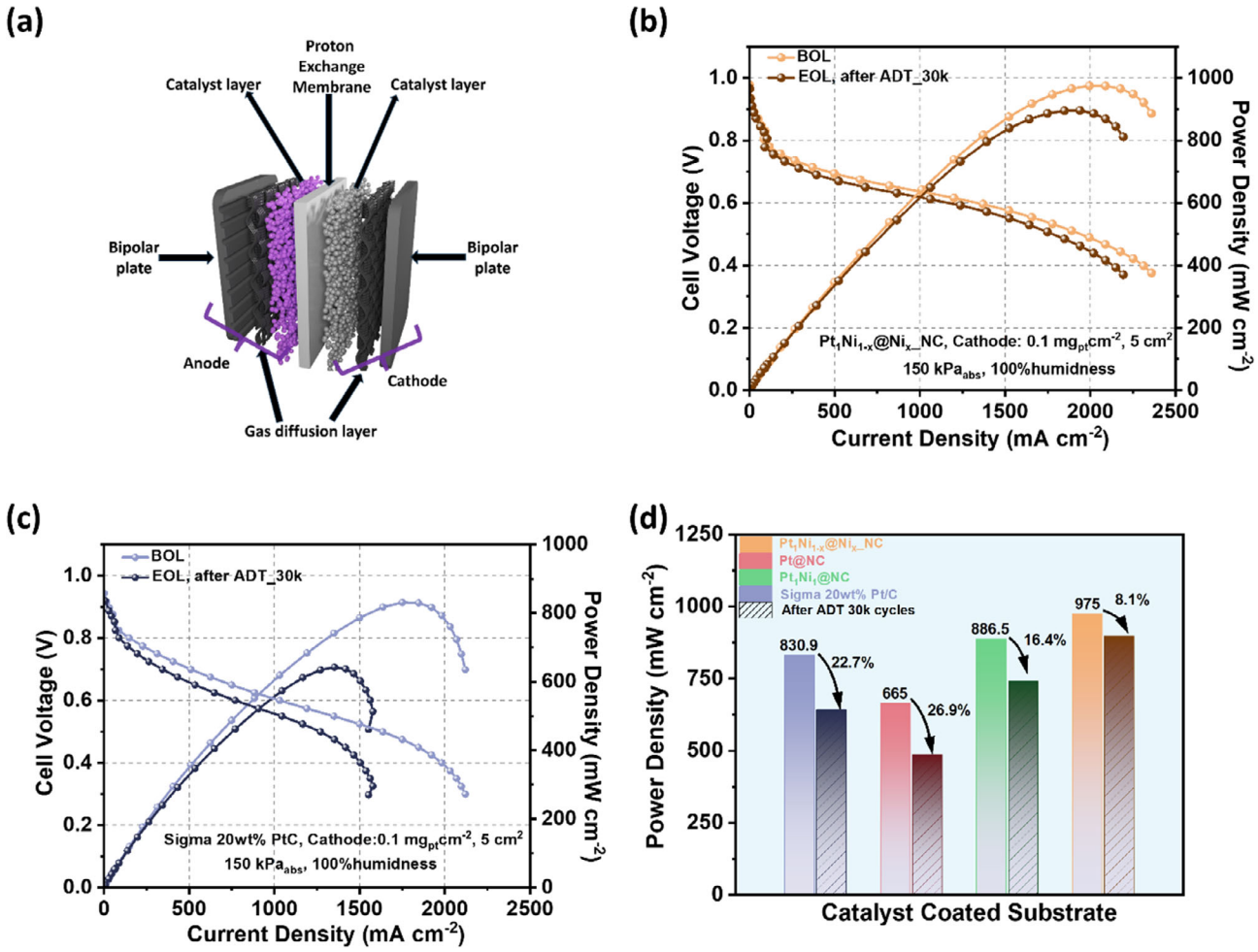


**FIGURE 5** | (a) Schematic illustration of the structural configuration of a fuel cell stack. (b) MEA performance of $Pt_1Ni_{1-x}@Ni_x$_NC cathode before (BOL) and after ADT (EOL) under the $H_2$/air condition. (c) MEA performance of Sigma 20 wt% Pt/C cathode before (BOL) and after ADT (EOL) under the $H_2$/air condition. (d) Peak power density of all tested MEA before and after ADT.

increased from 908 mW $cm^{-2}$ at 60% relative humidity to 975 mW $cm^{-2}$ at 100% (Figure S27). $Pt_1Ni_{1-x}@Ni_x$_NC also demonstrated remarkable cycling stability (Figure 5b), maintaining high performance without significant water flooding after 30,000 cycles, unlike commercial Pt/C (Figure 5c). This advantage is attributed to the present system; the Pt-rich shell ensures high intrinsic ORR activity and minimizes kinetic losses, thereby extending the operational regime toward mass-transport-limited conditions. Concurrently, the N-doped carbon framework and Ni–N/C moieties create polar interfacial domains and an interconnected porous architecture that promote efficient water removal and oxygen diffusion while preserving effective ionomer–catalyst contact. Together, these synergistic features alleviate transport-related limitations and underpin the high peak power density and stable performance at high current densities observed for $Pt_1Ni_{1-x}@Ni_x$_NC. Furthermore, Figure 5d illustrates that the peak power density retention from beginning-of-life (BOL) to end-of-life (EOL) was 91.9% (8.1% loss, Figure S28) for $Pt_1Ni_{1-x}@Ni_x$_NC, substantially outperforming Pt/C (22.7% loss, Figure S29), Pt@NC (26.7% loss, Figure S30), and $Pt_1Ni_1$@NC (16.4% loss, Figure S31). Notably, the achieved peak power density and durability rank among one of the highest reported for Pt-based catalysts under comparable MEA testing conditions (Table S12). These superior performances underscore the effectiveness of the controllable alloying–dealloying and confinement strategy, which enables a robust Pt-rich shell/ordered-alloy core configuration coupled with Ni–N/C interfacial sites, collectively stabilizing active centers and optimizing water management for long-term PEMFC operation.

## 3 | Conclusion

In summary, we establish a controllable alloying–dealloying strategy to construct PtNi nanoparticles confined within an N-doped carbon framework, yielding a $Pt_1Ni_{1-x}@Ni_x$_NC catalyst with a Pt-rich shell and stabilized Ni_NC structure. Ex-situ spectroscopic analyses reveal that selective dealloying tailors the Pt coordination environment and electronic structure, while the NC support reincorporates dissolved Ni, thereby suppressing agglomeration and enhancing durability. Consequently, $Pt_1Ni_{1-x}@Ni_x$_NC delivers exceptional ORR activity ($E_{1/2}$ = 0.932 V, mass activity 2.028 A $mgPt^{-1}$) and stability, with only a 6 mV loss in half-wave potential after 30,000 cycles. Beyond RDE tests, the catalyst demonstrates outstanding MEA performance under practical fuel-cell operating conditions (cathode catalyst loading: 0.1 $mg_{Pt}$ $cm^{-2}$, 80°C, 150 $kPa_{abs}$ backpressure). $Pt_1Ni_{1-x}@Ni_x$_NC achieves a peak power density of 975 mW $cm^{-2}$ at 100% RH and exhibits

remarkable cycling durability, retaining 91.9% of its beginning-of-life power density after 30,000 cycles, significantly outperforming commercial Pt/C and other PtNi benchmarks. In this work, the superior RDE activity of $Pt_1Ni_{1-x}@Ni_x$_NC, arising from its Pt-rich shell and optimized electronic structure, translates into reduced kinetic losses in MEA. Meanwhile, the N-doped carbon confinement and Ni–N/C moieties promote effective ionomer coverage, facilitate water evacuation, and maintain open gas-transport pathways. This synergy enables the intrinsic activity advantages observed in RDE tests to be preserved under practical PEMFC operating conditions.

Importantly, these results place $Pt_1Ni_{1-x}@Ni_x$_NC among the leading candidates for practical fuel-cell applications. Unlike conventional PtNi alloying or dealloying strategies that often suffer from Ni dissolution and nanoparticle coarsening under MEA conditions, the present alloying–dealloying–support coupling strategy resolves the long-standing trade-off between activity and stability. By simultaneously forming a Pt-rich shell and immobilizing released Ni as Ni–N/C moieties, a dual stabilization mechanism is established that preserves the optimized Pt electronic structure while effectively suppressing degradation pathways relevant to practical PEMFC operation. Looking forward, integrating such coordination and support-engineering strategies with advanced intermetallic ordering or dual-metal-site carbon supports may further mitigate transition-metal leaching and unlock the durability required for fuel cells and beyond.


### Acknowledgments

The authors would like to acknowledge UK Research and Innovation (UKRI) under the UK government's Horizon Europe funding guarantee (101077226; EP/Y008707/1) for funding support. This research also employed the resources of the B18 in the UK Diamond Light Source (BAG2023_SP34632-1), and many thanks to Dr. Martin Wilding, Dr. Simon Kondrat, and the Catalysis Hub BAG team for their kind help.


### Conflicts of Interest

The authors declare no conflicts of interest.

### Data Availability Statement

The data that support the findings of this study are available on request from the corresponding author. The data are not publicly available due to privacy or ethical restrictions.

### References


1. K. Jiao, J. Xuan, Q. Du, et al., "Designing the next Generation of Proton-Exchange Membrane Fuel Cells," *Nature* 595 (2021): 361–369, https://doi.org/10.1038/s41586-021-03482-7.

2. X. X. Wang, M. T. Swihart, and G. Wu, "Achievements, Challenges and Perspectives on Cathode Catalysts in Proton Exchange Membrane Fuel Cells for Transportation," *Nature Catalysis* 2 (2019): 578–589, https://doi.org/10.1038/s41929-019-0304-9.

3. J. Liang, H. Yu, M. J. Zachman, et al., "Creating Favorable Pt/Co Interfaces via a Two-Step Approach for Constructing Highly Durable PtCo Intermetallic Fuel Cell Catalysts," *Advanced Materials* 38 (2026): e10847.

4. C. Gyan-Barimah, J. S. P. Mantha, H. Y. Lee, et al., "High Vacancy Formation Energy Boosts the Stability of Structurally Ordered PtMg in Hydrogen Fuel Cells," *Nature Communications* 15 (2024): 7034, https://doi.org/10.1038/s41467-024-51280-2.

5. B. Peng, Z. Liu, L. Sementa, et al., "Embedded Oxide Clusters Stabilize Sub-2 Nm Pt Nanoparticles for Highly Durable Fuel Cells," *Nature Catalysis* 7 (2024): 818–828, https://doi.org/10.1038/s41929-024-01180-x.

6. M. Tang, H. Yan, X. Zhang, Z. Zheng, and S. Chen, "Materials Strategies Tackling Interfacial Issues in Catalyst Layers of Proton Exchange Membrane Fuel Cells," *Advanced Materials* 37 (2025): 2306387, https://doi.org/10.1002/adma.202306387.

7. L. Zhao, Z. Zhu, J. Wang, et al., "Unlocking Proton Exchange Membrane Fuel Cell Performance With Porous PtCoV Alloy Catalysts," *Advanced Materials* 37 (2025): 2502457, https://doi.org/10.1002/adma.202502457.

8. M. I. Maulana, J. Kim, H. Y. Lee, et al., "Magnetocrystalline Anisotropic Platinum–Palladium–Iron Ternary Intermetallic Alloy for Enhanced Fuel Cell Electrocatalysis," *Advanced Materials* 37 (2025): e10314, https://doi.org/10.1002/adma.202510314.

9. Y. Sun, Y. Lin, Z. Wan, et al., "Water Management and Performance Enhancement in Proton Exchange Membrane Fuel Cell Through Metal Foam Flow Field With Hierarchical Pore Structure," *Chemical Engineering Journal* 494 (2024): 152944, https://doi.org/10.1016/j.cej.2024.152944.

10. F. Calili-Cankir, E. M. Can, D. B. Ingham, et al., "Patterned Hydrophobic Gas Diffusion Layers for Enhanced Water Management in Polymer Electrolyte Fuel Cells," *Chemical Engineering Journal* 484 (2024): 149711, https://doi.org/10.1016/j.cej.2024.149711.

11. T. Chen, C. Qiu, X. Zhang, et al., "An Ultrasmall Ordered High-Entropy Intermetallic With Multiple Active Sites for the Oxygen Reduction Reaction," *Journal of the American Chemical Society* 146 (2024): 1174–1184, https://doi.org/10.1021/jacs.3c12649.

12. Y. Zeng, J. Liang, C. Li, et al., "Regulating Catalytic Properties and Thermal Stability of Pt and PtCo Intermetallic Fuel-Cell Catalysts via Strong Coupling Effects Between Single-Metal Site-Rich Carbon and Pt," *Journal of the American Chemical Society* 145 (2023): 17643–17655, https://doi.org/10.1021/jacs.3c03345.

13. F. Kong, Y. Huang, X. Yu, et al., "Oxygen Vacancy-Mediated Synthesis of Inter-Atomically Ordered Ultrafine Pt-Alloy Nanoparticles for Enhanced Fuel Cell Performance," *Journal of the American Chemical Society* 146 (2024): 30078–30090, https://doi.org/10.1021/jacs.4c07185.

14. W. Guo, X. Gao, M. Zhu, et al., "A Closely Packed $Pt_{1.5}Ni_{1-X}$ /Ni–N–C Hybrid for Relay Catalysis Towards Oxygen Reduction," *Energy & Environmental Science* 16 (2023): 148–156, https://doi.org/10.1039/D2EE02381D.

15. Q. Feng, X. Wang, M. Klingenhof, M. Heggen, and P. Strasser, "Low-Pt NiNC-Supported PtNi Nanoalloy Oxygen Reduction Reaction Electrocatalysts—In Situ Tracking of the Atomic Alloying Process," *Angewandte Chemie, International Edition in English* 61 (2022): e202203728, https://doi.org/10.1002/anie.202203728.

16. Y. Wu, L. Chen, S. Geng, et al., "PtFe Nanoalloys Supported on Fe-Based Cubic Framework as Efficient Oxygen Reduction Electrocatalysts for Proton Exchange Membrane Fuel Cells," *Advanced Functional Materials* 34 (2023): 2307297, https://doi.org/10.1002/adfm.202307297.

17. Z. Kong, Y. Maswadeh, J. A. Vargas, et al., "Origin of High Activity and Durability of Twisty Nanowire Alloy Catalysts Under Oxygen Reduction and Fuel Cell Operating Conditions," *Journal of the American Chemical Society* 142 (2020): 1287–1299, https://doi.org/10.1021/jacs.9b10239.

18. L. Du, V. Prabhakaran, X. Xie, S. Park, Y. Wang, and Y. Shao, "Low-PGM and PGM-Free Catalysts for Proton Exchange Membrane Fuel Cells: Stability Challenges and Material Solutions," *Advanced Materials* 33 (2021): 1908232, https://doi.org/10.1002/adma.201908232.

19. B. Wu, H. Yang, L. Li, et al., "Integrating PtCo Intermetallic With Highly Graphitized Carbon Toward Durable Oxygen Electroreduction in Proton Exchange Membrane Fuel Cells," *Advanced Materials* 37 (2025): 2500096, https://doi.org/10.1002/adma.202500096.

20. M. Zhu, H. Zhang, Y. Hu, et al., "In Situ Nitrogen Infiltration Into an Ordered $Pt_3Co$ Alloy With sp–d Hybridization to Boost Fuel Cell Performance," *ACS Catalysis* 14 (2024): 5858–5867, https://doi.org/10.1021/acscatal.3c06223.

21. Z. P. Wu, D. Dinh, Y. Maswadeh, et al., "Interfacial Reactivity-Triggered Oscillatory Lattice Strains of Nanoalloys," *Journal of the American Chemical Society* 146 (2024): 35264–35274, https://doi.org/10.1021/jacs.4c12550.

22. Z. Wang, S. Chen, W. Wu, et al., "Tailored Lattice Compressive Strain of Pt-Skins by the $L1_2$-$Pt_3M$ Intermetallic Core for Highly Efficient Oxygen Reduction," *Advanced Materials* 35 (2023): 2301310, https://doi.org/10.1002/adma.202301310.

23. J. Cui, D. Zhang, Z. Liu, et al., "Carbon-Anchoring Synthesis of $Pt_1Ni_1$@Pt/C Core-shell Catalysts for Stable Oxygen Reduction Reaction," *Nature Communications* 15 (2024): 9458, https://doi.org/10.1038/s41467-024-53808-y.

24. T. Zhao, M. Li, D. Xiao, et al., "Improving Alkaline Hydrogen Oxidation Through Dynamic Lattice Hydrogen Migration in Pd@Pt Core-Shell Electrocatalysts," *Angewandte Chemie, International Edition in English* 63 (2024): e202315148, https://doi.org/10.1002/anie.202315148.

25. J. Liang, Y. Wan, H. Lv, et al., "Metal Bond Strength Regulation Enables Large-Scale Synthesis of Intermetallic Nanocrystals for Practical Fuel Cells," *Nature Materials* 23 (2024): 1259–1267, https://doi.org/10.1038/s41563-024-01901-4.

26. L. Zhao, Z. Zhu, J. Wang, et al., "Robust p-D Orbital Coupling in PtCoIn@Pt Core–Shell Catalysts for Durable Proton Exchange Membrane Fuel Cells," *Angewandte Chemie, International Edition in English* 64 (2025): e202501805, https://doi.org/10.1002/anie.202501805.

27. S. Shin, E. Lee, J. Nam, et al., "Carbon-Embedded Pt Alloy Cluster Catalysts for Proton Exchange Membrane Fuel Cells," *Advanced Energy Materials* 14 (2024): 2400599, https://doi.org/10.1002/aenm.202400599.

28. Z. Tian, Q. Zhang, L. Thomsen, et al., "Constructing Interfacial Boron-Nitrogen Moieties in Turbostratic Carbon for Electrochemical Hydrogen Peroxide Production," *Angewandte Chemie, International Edition in English* 61 (2022): e202206915, https://doi.org/10.1002/anie.202206915.

29. Z. Yang, G. Hou, N. Gao, et al., "Histidine-Based , "Transfer Stations" at Carbon-Immobilized Metal Particles Enable Rapid Hydrogen Transfer for Efficient Formic Acid Dehydrogenation," *Angewandte Chemie, International Edition in English* 64 (2025): e202501836, https://doi.org/10.1002/anie.202501836.

30. B. X. Yu, W. J. Niu, C. Y. Cai, L. Y. Xu, and F. M. Wang, "Advances and Directions of Ordered Pt-Based Transition Metal Alloys Supported on Carbon With Different Dimensions for Boosting ORR Catalytic Activity Toward PEMFCs," *Advanced Functional Materials* 36 (2025): e12569, https://doi.org/10.1002/adfm.202512569.

31. Y. Chen, Z. Meng, X. Wei, et al., "Tellurium–Nitrogen–Carbon Support Boosting Platinum Catalysis in High-Efficiency Proton Exchange Membrane Fuel Cells," *Angewandte Chemie, International Edition in English* 137 (2025): e202512315, https://doi.org/10.1002/ange.202512315.

32. Z. Shi, Y. Wang, J. Li, et al., "Confined Ir Single Sites With Triggered Lattice Oxygen Redox: Toward Boosted and Sustained Water Oxidation Catalysis," *Joule* 5 (2021): 2164–2176, https://doi.org/10.1016/j.joule.2021.05.018.

33. N. Zhao, W. Luo, S. Li, et al., "Strong Bonding of Lattice N Activates Metal Ni to Achieve Efficient Water Splitting," *Advancement of Science* 12 (2025): 2411526, https://doi.org/10.1002/advs.202411526.

## Supporting Information

Additional supporting information can be found online in the Supporting Information section.

**Supporting File 1**: anie71482-sup-0001-SuppMat.docx.